Pattern Recognition 58 (2016) 1–11

Contents lists available at ScienceDirect

Pattern Recognition

journal homepage: www.elsevier.com/locate/pr

Segmentation of cell nuclei in fluorescence microscopy images: An integrated framework using level set segmentation and touching-cell splitting

Amin Gharipour *, Alan Wee-Chung Liew

School of Information and Communication Technology, Gold Coast Campus, Griffith University, QLD4222, Australia

ARTICLE INFO

Article history:
Received 21 July 2015
Received in revised form
30 January 2016
Accepted 28 March 2016
Available online 6 April 2016

Keywords:
Fluorescence microscopy images
Level set segmentation
Touching-cell splitting

ABSTRACT

Accurate segmentation of cells in fluorescence microscopy images plays a key role in high-throughput applications such as quantification of protein expression and the study of cell function. In this paper, an integrated framework consisting of a new level sets based segmentation algorithm and a touching-cell splitting method is proposed. For cell nuclei segmentation, a new region-based active contour model in a variational level set formulation is developed where our new level set energy functional minimizes the Bayesian classification risk. For touching-cell splitting, the touching cells are first distinguished from non-touching cells, and then a strategy based on the splitting area identification is proposed to obtain splitting point-pairs. To form the appropriate splitting line, the image properties from different information channels are used to define the surface manifold of the image patch around the selected splitting point-pairs and geodesic distance is used to measure the length of the shortest path on the manifold connecting the two splitting points. The performance of the proposed framework is evaluated using a large number of fluorescence microscopy images from four datasets with different cell types. A quantitative comparison is also performed with several existing segmentation approaches.

1. Introduction

Numerous areas of analysing and quantifying fluorescence microscopy images rely on quantitative cell nucleus image analysis [1–3]. Specifically, the basis for all automatic image analysis required in high-throughput applications is cell image segmentation. Semi-automatic and manual segmentation methods are tedious, need intensive labor, and suffer from inter-and intra-reader variability. Therefore automatic methods with the ability to deal with different cell types and image artifacts are required.

Specifically, this paper has two main goals. The first goal is motivated by the fact that in cell nuclei image segmentation, pixels in an image patch possess nearly the same intensity. Therefore, the spatial relationship of the pixels in an image patch can be utilized as an important characteristic that improves the performance of level set segmentation methods [4–7]. Consequently, the first goal is to develop a segmentation algorithm based on the image patch information [8–11]. The segmentation algorithms often fail to separate the individual cells which form clumps. Since quantitative cell nucleus image analysis is dependent on the characteristics of each individual cell, the overlapping of cells could have an adverse effect on the performance of the quantitative high-throughput automated image analysis. Thus, the second goal is to develop a splitting algorithm for touching cells.

The contributions of this paper are as follows. 1) A new approach is introduced for cell nucleus segmentation in fluorescence microscopy images. First, a region-based active contour model in a variational level set formulation, which is based on the image patch information, is used to segment the image. Compared to previous approaches, we define a novel local energy functional based on the Bayesian classification risk [12–14] for an image patch. In addition, a weighting scheme is used to enable the pixels in each image patch to have anisotropic weights. 2) A three-step touching-cell splitting algorithm is utilized for splitting. In the first step, morphological features, and the distance between the most likely radial-symmetry point and the geometrical center, are utilized to distinguish touching-cell clumps from non-touching cells. After touching-cell identification, splitting areas are identified, and pairs of splitting points are selected for each clump. Once the splitting points are recognized, the image patch around splitting points is defined as their joint neighborhood. The image properties from different information channels are used to define the surface manifold of the image patch, and geodesic distance is used to

* Corresponding author.
E-mail addresses: amin.gharipour@griffithuni.edu.au (A. Gharipour), a.liew@griffith.edu.au (A. Liew).

http://dx.doi.org/10.1016/j.patcog.2016.03.030
0031-3203/

measure the length of the shortest path on the manifold connecting the two splitting points. Finally, Dijkstra's algorithm [15] is used to find the weighted shortest path between splitting points.

The remainder of this paper is organized as follows. Section 2 introduces the proposed approaches. In Section 3, experimental results are presented and analysed using different cell types. The results of the proposed methods are also compared with previous approaches. This paper is summarized in Section 4.

2. Proposed approach

2.1. Background

Recently, many methods have been proposed for the segmentation of cell nuclei in fluorescence microscopy images. One of the most common approaches for cell segmentation is intensity thresholding which suffers from intensity inhomogeneity. Watershed-based methods are commonly utilized for clustered nuclei separation. A cell segmentation method based on the watershed algorithm and the cluster splitting technique has been introduced in [1]. A method based on the improved distance transform and statistical model-based merging has been proposed in [2]. Marker-controlled watershed techniques are proposed by Cheng and Rajapakse [3] as well as Jung and Kim [16] for cluster splitting, where the H-minima transform is used to find the optimal number of markers.

Deformable models, which are able to capture a wide spectrum of different shapes, can be considered as a major category of cell segmentation techniques. There are two main types of deformable models: parametric models [17], which use an explicit representation of objects [18–20], and implicit models [21]. A region based parametric energy functional is introduced in [18]. Their proposed model utilizes a coupling term for multiple contours as well as a penalty term to prevent merging. In [19], the authors used texture-adaptive weights to overcome the internal pseudo-edges and low-contrast cell boundaries problems of Zimmer and Olivo-Marin's model [18]. Butenuth and Heipke proposed a method for image segmentation which was based on the parametric active contour model and a graph-based approach [20]. Although parametric active contour models can be considered as one of the common approaches for image segmentation, these models depend on the parameterization and are not able to deal with topological changes.

Implicit models [6,7,22–42] using level sets have been widely used in cell segmentation with promising results. The implicit models are able to handle topological changes, which are typically not possible in parametric models. A two-step level set method has been developed for cell segmentation in [29]. An energy functional which is based on the multiple active contours integration as well as a combination of gradient based and region-based terms has been introduced in [30]. In [13], Voronoi tessellation has been utilized to determine regions corresponding to single cells and then for each of these regions, region based energy functional is used. In [14], the flux tensor is used for initialization of their proposed level set method which was based on Bayesian energy functional. The cell and the background of cell images are separated using a gradient-based level set approach and then topology preserving level sets are employed to perform cluster splitting in [16]. A level set method based on Bayesian energy functional which uses a non-PDE-based minimization is developed in [39]. For cell image segmentation, the level set methods and the graph partitioning approaches have been combined within in a variational framework in [38,40]. Sequential integrations of fuzzy clustering and implicit models have been proposed in [43–45]. A multi-phase graph partitioning active contour approach which uses regional density functions has been developed in [38]. A two-step level set method for histopathological images has been proposed in [40] where first, a geodesic active contour model is initialized using a hierarchical normalized cuts scheme and then a level set functional is used. An approach has been proposed in [46] for segmenting cell nuclei s based on active contours using level sets and convex energy functionals.

2.2. Local level set method based on the Bayesian risk and weighted image patch (LLBWIP)

2.2.1. Modeling

Assuming that an image is formed by two regions, cell and background pixels, the following two hypotheses can be used to characterize the image segmentation.

- A null hypothesis H_1, in which the cell is absent.
- An alternative hypothesis H_2, in which the cell is present.

The segmentation method is utilized to decide which hypothesis is correct. Therefore, one of two decisions can be made:

- D_1: the classifier declares that the cell is absent.
- D_2: the cell is present, and thus should be chosen by segmentation procedure.

The following four conditional probabilities are defined for the combinations of decisions in the hypothesis test:

(1) $P(D_1|H_1)$ is the probability of declaration that the cell is absent when it is actually absent.
(2) $P(D_2|H_1)$ is the probability of declaration that the cell is present when it is absent.
(3) $P(D_1|H_2)$ is the probability of declaration that the cell is absent when it is present.
(4) $P(D_2|H_2)$ is the probability of declaration that the cell is present when it is actually present.

Using the statistical terminology, the first probability, which is the probability of rejecting the null hypothesis H_1 when it is actually true, is called *type I* risk. On the other hand, $P(D_1|H_2)$, which can be considered the probability of accepting H_1 when H_1 is actually false, is called *type II* risk. The consequence of each combination of hypothesis and decision is quantified with an associated loss. The losses of $P(D_1|H_1)$, $P(D_2|H_1)$, $P(D_1|H_2)$, and $P(D_2|H_2)$ can be denoted as $L(1,1)$, $L(2,1)$, $L(1,2)$, and $L(2,2)$, respectively. $L(1,1)$ and $L(2,2)$ can be viewed as the losses arising from the correct decision while $L(2,1)$ and $L(1,2)$ denote the losses that arise from the incorrect decision. As the general rule, we set $L(1,1)=L(2,2)=0$ and $L(2,1)=L(1,2)=1$ [12]. Now the Bayesian risk for segmenting an image into cell and background can be written as follows:

$$r = P(H_1)P(D_2|H_1)+P(H_2)P(D_1|H_2) \quad (1)$$

Assuming $\Omega = \Omega_{i=1}^{2}$ denotes the image domain, where Ω_1 and Ω_2 denote cell and background pixels, respectively. $I:\Omega \rightarrow \mathbb{R}^{+}$ denotes a given image, for each point $\mathbf{x}$ in the image domain Ω, the image patch centered on $\mathbf{x}$ can be represented as:

$$P_{\mathbf{x}} = (I(\mathbf{y}), \mathbf{y} \in N_{\mathbf{x}}) \quad (2)$$

where $N_{\mathbf{x}}$ can be considered as a $q \times q$ neighbourhood of point $\mathbf{x}$. Now the image patch $P_{\mathbf{x}}$ with domain $N_{\mathbf{x}}$ can be partitioned by $\Omega_{i=1}^{2}$ into the following disjoint regions:

$R_1 = \{\Omega_1 \cap N_{\mathbf{x}}\}$ and $R_2 = \{\Omega_2 \cap N_{\mathbf{x}}\}$, where $N_{\mathbf{x}} = \cup_{i=1}^{2} R_i, R_i \cap R_j = \varnothing \forall i \neq j$.

D_1 and D_2 can now be redefined as follows; all pixels of the image patch $P_{\mathbf{x}}$ that lead the segmentation procedure to choose

decision D_1 fall in the region R_1, whereas all pixels of the image patch $P_{\mathbf{x}}$ that result in decision D_2 fall in the region R_2. The two hypotheses, H_1 and H_2, are considered in association with pdfs $P(I(\mathbf{x})|H_1)$ and $P(I(\mathbf{x})|H_2)$, respectively, where $I(\mathbf{x})$ denotes a pixel value of the $N_{\mathbf{x}}$. The integral of $P(I(\mathbf{x})|H_1)$ over the region R_2 represents the risk $P(D_2|H_1)$ and the integral of $P(I(\mathbf{x})|H_2)$ over the region R_1 represents the risk$P(D_1|H_2)$. Now the energy functional, based on the Bayesian risk for segmenting an image patch $P_{\mathbf{x}}$ into cell and background, can be written as follows:

$$E_{\mathbf{x}} = e_1 + e_2 \tag{3}$$

where e_1 and e_2 are defined as follows:

$$\begin{cases} e_1 = \int_{R_1} \ln\left(P(I(\mathbf{y})|\mathbf{y} \in R_2)P(\mathbf{y} \in R_2)\right)d\mathbf{y} \\ e_2 = \int_{R_2} \ln(P(I(\mathbf{y})|\mathbf{y} \in R_1)P(\mathbf{y} \in R_1))d\mathbf{y} \end{cases} \tag{4}$$

Since dissimilar pixels should have different weights to reflect their decrease of importance [47–50], a weighting function needs to be defined and incorporated into (4) to constrain the influence of dissimilar pixels. To define the weighting function for each pixel $\mathbf{y}$, first, its mean square deviation $\sigma_{\mathbf{yx}}$ is calculated as follows:

$$\sigma_{\mathbf{yx}} = \left(\frac{\int_{\mathbf{y}' \in N_{\mathbf{x}}/\mathbf{y}} (I(\mathbf{y}') - I(\mathbf{y}))^2}{n_{\mathbf{x}} - 1}\right)^{\frac{1}{2}} \tag{5}$$

Then, the following exponential kernel function is utilized to produce the weight for pixel $\mathbf{y}$:

$$\zeta_{\mathbf{yx}} = \exp\left(-\left(\sigma_{\mathbf{yx}} - \frac{\int_{\mathbf{y} \in N_{\mathbf{x}}} \sigma_{\mathbf{yx}}}{n_{\mathbf{x}}}\right)\right) \tag{6}$$

Finally, the weights are normalized by:

$$\kappa_{\mathbf{yx}} = \frac{\zeta_{\mathbf{yx}}}{\int_{\mathbf{y} \in N_{\mathbf{x}}} \zeta_{\mathbf{yx}}} \tag{7}$$

The weighting function can now be defined as follows:

$$\omega_{\mathbf{y}} = \begin{cases} \kappa_{\mathbf{yx}}, & for \quad I(\mathbf{y}) \in P_{\mathbf{x}} \\ 0, & for \quad I(\mathbf{y}) \notin P_{\mathbf{x}} \end{cases} \tag{8}$$

It is noted that $\omega_{\mathbf{y}}$ is well defined on the $N_{\mathbf{x}}$ and $\int_{N_{\mathbf{x}}} \omega_{\mathbf{y}} d\mathbf{y} = 1$. With this weighting function, for $\mathbf{y} \in N_{\mathbf{x}}$ if the mean square deviation of $I(\mathbf{y})$is far away from the average mean-square deviation in the $P_{\mathbf{x}}$, $I(\mathbf{y})$ is expected to have a very small weight. The calculated weight vectors of two different image patches are shown in Fig. 1. The pixel values in both patches are given in the first column. The mean square deviations $\sigma_{\mathbf{yx}}$ are given in the middle column and the right column shows the obtained weights. The first image patch (the upper row) is selected from the boundary area while the second image patch (the bottom row) is selected from the homogeneous area. In the first patch, the weight of the pixel with high intensity (over 200) inclines to zero. Also in this patch the pixels with intensity values 49 and 81 are considered as noisy pixels. In the second image patch, pixels with intensity values 81, 80, 161 and 164 are all considered as noise and their weights also incline to zero. As can be seen from the calculated weight vectors in both examples, the anisotropic weighting method can effectively reduce the impact of edges and noisy pixels on images. Using this weighting function, (4) is reformulated as:

$$\begin{cases} e_1 = \int_{\Omega_1} \omega_{\mathbf{y}} \ln\left(P(I(\mathbf{y})|\mathbf{y} \in R_2)P(\mathbf{y} \in R_2)\right)d\mathbf{y} \\ e_2 = \int_{\Omega_2} \omega_{\mathbf{y}} \ln\left(P(I(\mathbf{y})|\mathbf{y} \in R_1)P(\mathbf{y} \in R_1)\right)d\mathbf{y} \end{cases} \tag{9}$$

Assuming that $P(I(\mathbf{y})|\mathbf{y} \in R_2)$ and $P(I(\mathbf{y})|\mathbf{y} \in R_1)$ follow the Gaussian distribution, (9) can be written as follows:

$$\begin{cases} e_1 = \int_{\Omega_1} \omega_{\mathbf{y}} \ln\left(\mathcal{N}(I(\mathbf{y})|\mu_2(\mathbf{y}), \sum_2(\mathbf{y}))P(\mathbf{y} \in R_2)\right)d\mathbf{y} \\ e_2 = \int_{\Omega_2} \omega_{\mathbf{y}} \ln\left(\mathcal{N}(I(\mathbf{y})|\mu_1(\mathbf{y}), \sum_1(\mathbf{y}))P(\mathbf{y} \in R_1)\right)d\mathbf{y} \end{cases} \tag{10}$$

where $\mu_i(\mathbf{y})$ and $\sum_i(\mathbf{y})$ denote the mean and the covariance matrix, respectively, of the Gaussian distribution.

To consider the bias field that corrects for the intensity inhomogeneity into the energy functional $E_{\mathbf{x}}$, assuming that the true intensity v_i in each region R_i is constant, $\mu_i(\mathbf{y})$ can be approximated as follows [48,49]:

$$\mu_i(\mathbf{y}) = b(\mathbf{y})v_i \quad for \quad i = 1, 2. \tag{11}$$

where $b(\mathbf{y})$ denotes the bias field at each pixel. Therefore, (10) can be reformulated as:

$$\begin{cases} e_1 = \int_{\Omega_1} \omega_{\mathbf{y}} \ln\left(\mathcal{N}(I(\mathbf{y})|b(\mathbf{y})v_2, \sum_2(\mathbf{y}))P(\mathbf{y} \in R_2)\right)d\mathbf{y} \\ e_2 = \int_{\Omega_2} \omega_{\mathbf{y}} \ln\left(\mathcal{N}(I(\mathbf{y})|b(\mathbf{y})v_1, \sum_1(\mathbf{y}))P(\mathbf{y} \in R_1)\right)d\mathbf{y} \end{cases} \tag{12}$$

Two prior probabilities $P(\mathbf{y} \in R_2)$ and $P(\mathbf{y} \in R_1)$ are still unknown. Although it can be assumed that the prior probabilities are equal for both regions [51], an iterative algorithm derived from the concavity of the Kullback–Leibler information number is adopted for prior probabilities estimation [14,52]. Finally, the aim is to find the energy for all the centre points $\mathbf{x}$ in the image domain Ω, therefore $E_{LLBWIP} = \int_{\Omega} E_{\mathbf{x}} d\mathbf{x}$ denotes the final energy functional.

2.2.2. Level set formulation

We assume that the two regions R_1 and R_2 can be represented by the regions separated by the Lipchitz function $\varnothing$, $\Omega_1 = \{\varnothing(\mathbf{x}) > 0\}$ and $\Omega_2 = \{\varnothing(\mathbf{x}) \le 0\}$. By incorporating the Heaviside function H, e_1

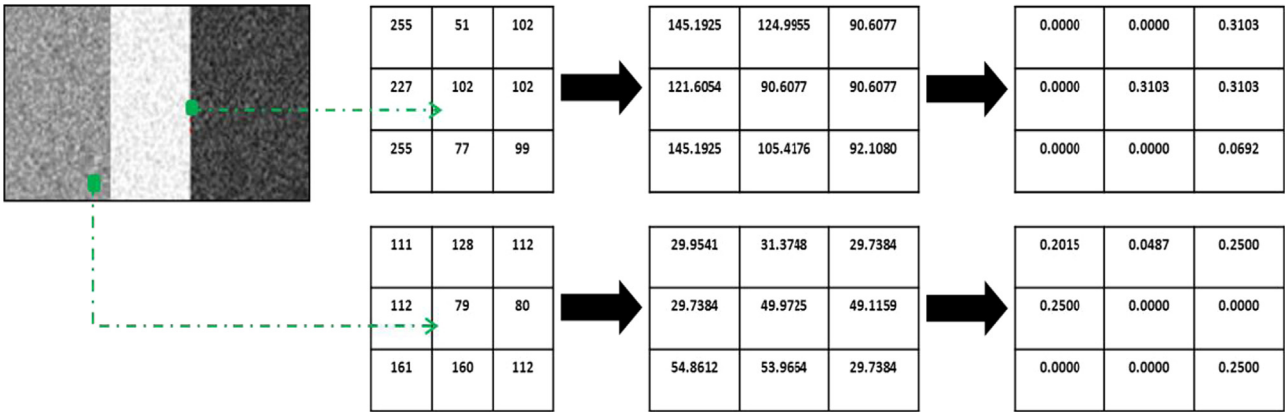

Fig. 1. Two image patches selected from a synthetic image, (middle column) the calculated mean-square deviation and (right column) the estimated weight vectors.

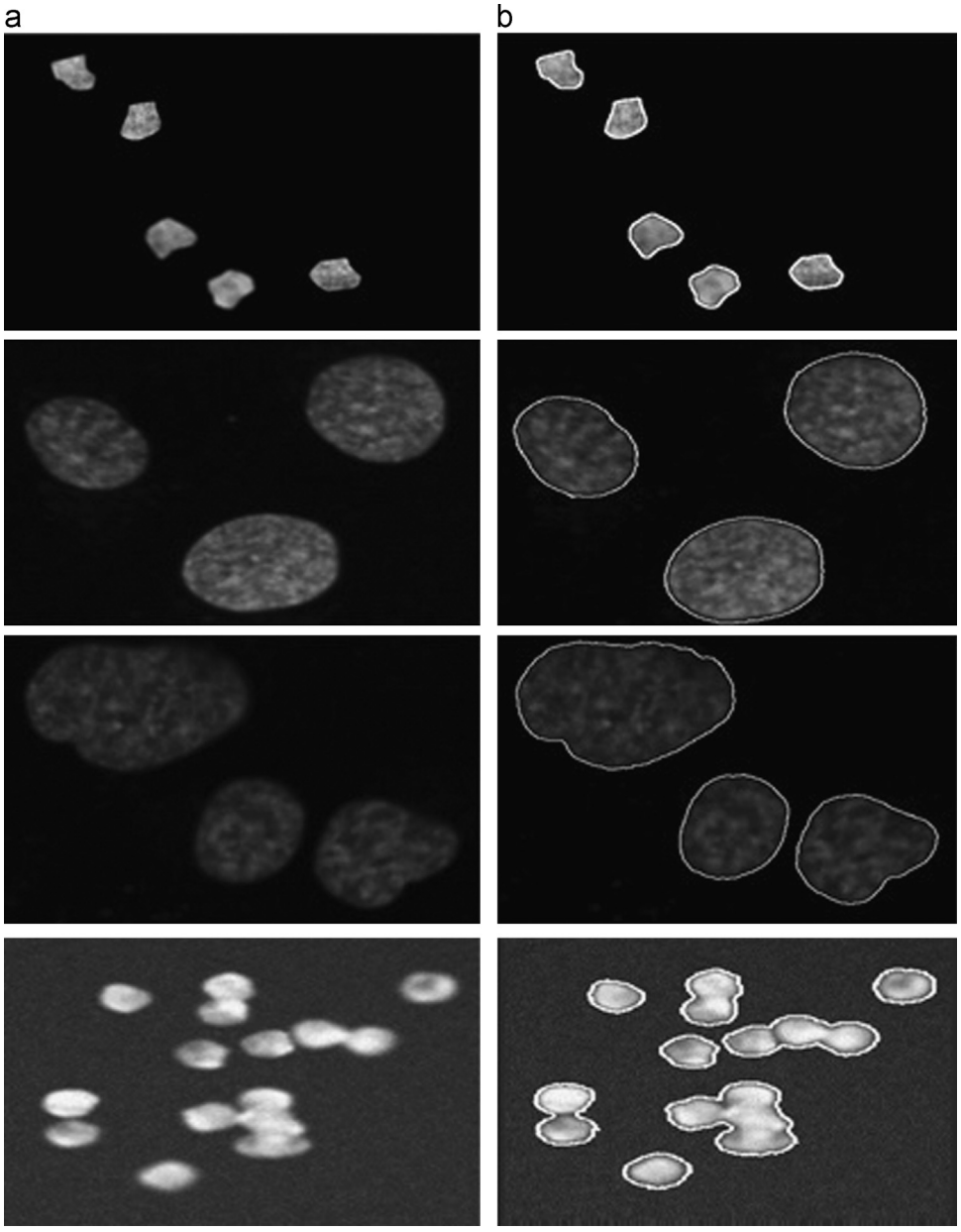

Fig. 2. Segmentation results of the proposed approach. Column (a) original images. Column (b) segmentation results of the proposed functional.

and e_2 are rewritten as follows:

$$\begin{cases} e_1 = \int_\Omega \omega_{\mathbf{y}} \ln\ \left(\mathcal{N}(\mathrm{I}(\mathbf{y})|\mathrm{b}(\mathbf{y})\mathrm{v}_2, \sum_2(\mathbf{y}))\mathrm{P}(\mathbf{y}\in \mathrm{R}_2)\mathrm{M}_1(\varnothing(\mathbf{y}))\right)\mathrm{d}\mathbf{y} \\ e_2 = \int_\Omega \omega_{\mathbf{y}} \ln\ \left(\mathcal{N}(\mathrm{I}(\mathbf{y})|\mathrm{b}(\mathbf{y})\mathrm{v}_1, \sum_1(\mathbf{y}))\mathrm{P}(\mathbf{y}\in \mathrm{R}_1)\mathrm{M}_2(\varnothing(\mathbf{y}))\right)\mathrm{d}\mathbf{y} \end{cases} \tag{13}$$

where $\mathrm{M}_1(\varnothing(\mathbf{y})) = \mathrm{H}(\varnothing(\mathbf{y}))$ and $\mathrm{M}_2(\varnothing(\mathbf{y})) = 1 - \mathrm{H}(\varnothing(\mathbf{y}))$.

Therefore, the energy functional $\mathrm{E}_{\mathrm{LLBWIP}}$ can be rewritten as follows:

$$\mathrm{E}_{\mathrm{LLBWIP}} = \int_\Omega (e_1) + e_2)\mathrm{d}\mathbf{x} + \gamma\mathcal{L}() + \mathcal{P}() \tag{14}$$

where $\mathcal{L}()$ and $\mathcal{P}()$ are defined as follows:

$$\begin{cases} \mathcal{L}(\varnothing(\mathbf{x})) = \int_\Omega \delta(\varnothing)|\nabla(\varnothing)|\mathrm{d}\mathbf{x} \\ \mathcal{P}(\varnothing(\mathbf{x})) = \int_\Omega \frac{1}{2}(|\nabla\varnothing(-1)^2\mathrm{d}\mathbf{x} \end{cases} \tag{15}$$

where $\delta(\mathrm{z}) = \frac{\partial \mathrm{H}(\mathrm{z})}{\partial \mathrm{z}}$ and $\mathcal{L}()$ is used to control the smoothness of the zero level set and avoids the formation of small, isolated regions in the final segmentation. $\mathcal{P}()$ is used to eliminate the need for re-initialization in our method [7]. The parameter γ can be understood as the parameter which controls the penalization effect of the length term. For small γ, smaller objects will be detected while for large values of γ, larger objects will be detected. In this work, γ is set to $255\times255\times10^{-3}$. The Heaviside function $\mathrm{H}(\mathrm{z})$ can be approximated by a smooth function $H_\varepsilon(\mathrm{z})$, which is defined as:

$$\mathrm{H}_\varepsilon(\mathrm{z}) = \frac{1}{2}\left[1 + \frac{2}{\pi}\arctan\left(\frac{\mathrm{z}}{\varepsilon}\right)\right] \tag{16}$$

where ε is a positive constant (see Fig. 3). Therefore, the energy functional is approximated as follows:

$$\mathrm{E}_{\mathrm{LLBWIP}\varepsilon} = \int_\Omega (e_{1\varepsilon}) + e_{2\varepsilon})\mathrm{d}\mathbf{x} + \gamma\mathcal{L}_\varepsilon() + \mathcal{P}() \tag{17}$$

where $e_{1\varepsilon}$, $e_{2\varepsilon}$, and $\mathcal{L}_\varepsilon(\varnothing)$ approximate e_1, e_2, and $\mathcal{L}()$, respectively. Fig. 2 shows visual examples of the segmentation results for the proposed functional.

2.2.3. Minimization

In numerical implementation, for fixed $\varnothing$ and $i=1,2$, the variables $\sum_i(y)$, b(y), and v_i are updated as follows:

$$\sum_i(\mathbf{y})=\frac{\int_\Omega \omega_{\mathbf{y}}(I(\mathbf{y})-b(\mathbf{y})v_i)^2 P(\mathbf{y}\in R_i)M_{i,\epsilon}(\varnothing(\mathbf{y})))d\mathbf{y}}{\int_\Omega \omega_{\mathbf{y}} P(\mathbf{y}\in R_i)M_{i,\epsilon}(\varnothing(\mathbf{y})))d\mathbf{y}} \tag{18}$$

$$b(\mathbf{y})=\frac{\sum_{i=1}^{2}\int_\Omega \omega_{\mathbf{y}}(I(\mathbf{y})\sum_i(\mathbf{y})^{-1}v_i)P(\mathbf{y}\in R_i)M_{i,\epsilon}(\varnothing(\mathbf{y})))d\mathbf{y}}{\sum_{i=1}^{2}\int_\Omega \omega_{\mathbf{y}}(v_i(\mathbf{y})\sum_i(\mathbf{y})^{-1}v_i)P(\mathbf{y}\in R_i)M_{i,\epsilon}(\varnothing(\mathbf{y})))d\mathbf{y}} \tag{19}$$

$$v_i=\frac{\int_\Omega \omega_{\mathbf{y}} b(\mathbf{y})\sum_i(\mathbf{y})^{-1}P(\mathbf{y}\in R_i)I(\mathbf{y})M_{i,\epsilon}(\varnothing(\mathbf{y}))d\mathbf{y}}{\int_\Omega \omega_{\mathbf{y}} b(\mathbf{y})^2\sum_i(\mathbf{y})^{-1}P(\mathbf{y}\in R_i)M_{i,\epsilon}(\varnothing(\mathbf{y}))d\mathbf{y}} \tag{20}$$

Minimization of the energy functional E_ε with respect to $\varnothing$ is achieved by solving the following gradient descent flow equation:

$$\frac{\partial\varnothing}{\partial t}=\delta_\varepsilon(\varnothing)\mathcal{F}+\left(\nabla^2\varnothing-\mathrm{div}\left(\frac{\nabla\varnothing}{|\nabla\varnothing|}\right)\right) \tag{21}$$

where $\mathcal{F}$ is defined as:

$$\begin{aligned}\mathcal{F}=&\left(\int_\Omega \omega_{\mathbf{y}}P(\mathbf{y}\in R_2)\left(\ln\left(\sum_2(\mathbf{y})\right)+\frac{(I(\mathbf{y})-b(\mathbf{y})v_2)^2}{\sum_2(\mathbf{y})}\right)d\mathbf{y}\right)\\&-\left(\int_\Omega \omega_{\mathbf{y}}P(\mathbf{y}\in R_1)\left(\ln\left(\sum_1(\mathbf{y})\right)+\frac{(I(\mathbf{y})-b(\mathbf{y})v_1)^2}{\sum_1(\mathbf{y})}\right)d\mathbf{y}\right)\\&+\gamma\ \mathrm{div}\left(\frac{\nabla\varnothing}{|\nabla\varnothing|}\right)\end{aligned} \tag{22}$$

The parameter ε can affect the speed function. As can be seen in Fig. 3, for the large value of ε, for instance, $\varepsilon=4$, the weight $\delta_\varepsilon(\varnothing)$ becomes very small and consequently $\delta_\varepsilon(\varnothing)\mathcal{F}$ in (21) is trivial while for the small values of ε, for example, $\varepsilon=0.1$, only a very small range of level sets is weighted. The convergence of the energy minimization is slowed down by both cases and therefore, practically, ε is set to 1 or 1.5 [22,53].

2.3. Touching cell splitting

2.3.1. Detection of touching cells

In contrast to most available cell splitting methods, in this paper the touching and non-touching cells are separated and then the cell splitting procedure is only used for the touching cells [54]. The splitting algorithm consists of three steps as summarized by the flowchart in Fig. 4. In our approach, first, a measurement of the convex hull of the segmented image coupled with the use of the radial symmetry point detector [55] are applied to a connected region $\varkappa_i$ of the segmented image to define two decision variables, $\mathfrak{D}_1$ and $\mathfrak{D}_2$. Then $\mathfrak{D}_1$ and $\mathfrak{D}_2$ are used to determine whether $\varkappa_i$ is a single cell or a clump of touching cells.

To find the most likely radial symmetry centre r_i, the radial symmetry point detector [28] is applied to $\varkappa_i$. Let the geometrical centre of the $\varkappa_i$ be given by g_i and r_i denotes the pixel with the maximum value in the symmetry transform of the image [55], $\mathfrak{D}_1$ can be defined as follows:

$$\mathfrak{D}_1=\begin{cases}1 & \text{if } |r_i-g_i|>y_1\\ 0 & \text{otherwise}\end{cases} \tag{23}$$

where y_1 denotes a threshold of the distance between the radial-symmetry centre and geometrical centre of $\varkappa_i$. Practically, y_1 is set to six pixels.

The area of the convex hull of $\varkappa_i$ and the area of $\varkappa_i$ are denoted by A_v and A_c, respectively. Now $\mathfrak{D}_2$ can be defined as follows:

$$\mathfrak{D}_2=\begin{cases}1 & \frac{A_c}{A_v}<y_2\\ 0 & \text{otherwise}\end{cases} \tag{24}$$

where y_2 denotes a threshold of the ratio of $\frac{A_c}{A_v}$ and is set to

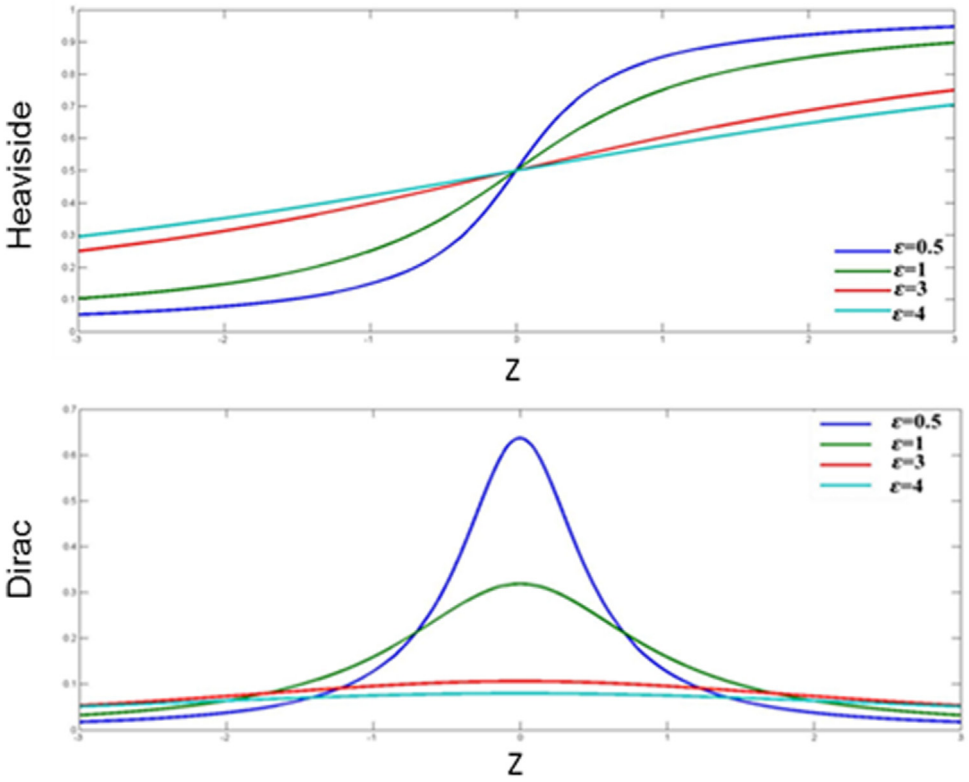

Fig. 3. The Heaviside function and the Dirac delta function with different ε values.

92×10^{-2}. $\varkappa_i$ can be considered as a touching cell if the following condition is satisfied:

$$\varkappa_i = \begin{cases} \text{touching cell clump} & \text{if} \quad \mathfrak{D}_1 = 1 \quad \text{or} \quad \mathfrak{D}_2 = 1 \\ \text{non touching cell clump} & \text{otherwise} \end{cases} \tag{25}$$

2.3.2. Candidate points for cell splitting

We describe here the second step of the proposed three-step cell splitting algorithm, known as splitting point-pair identification for splitting. In this paper, for a given clump to split,$\mathbb{C}_i$, it has been assumed that touching clump $\mathbb{C}_i$ has roughly a convex shape [56,57]. Let splitting area (such as hatched regions in Fig. 5),$SA_{\mathbb{C}_i}$, be defined as a difference of the convex hull region of $\mathbb{C}_i$ (such as dashed green line in Fig. 5) and $\mathbb{C}_i$. Therefore,$SA_{\mathbb{C}_i} = \{\cup_{\mathbb{k}=1}^{\mathbb{K}} SA_{\mathbb{C}_i\mathbb{k}}\}$, where $\mathbb{k} = \{1, \ldots, \mathbb{K}\}$ and $\mathbb{K}$ is the total number of splitting areas for $\mathbb{C}_i$. For example for Fig. 5(a), since the given clump has four splitting areas, $\mathbb{K} = 4$. For each splitting area, first, the associated directional vector (Blue arrows in Fig. 5(b)) is defined as a vector with its tail on the midpoint of the imaginary local chord (such as the dashed black line in Fig. 5(b)), and initiating towards the splitting area [58]. After finding the associated directional vector, we select two points on the tails of local chord (such as the blue circles in Fig. 5(b)). Then, two lines are initiated from the selected points and extended on either side using the directional vector (such as the dashed brown line in Fig. 5(b)) until the lines intersect the contour of $\mathbb{C}_i$ (such as the black circles in Fig. 5(b)). $\mathbb{F}_{\mathbb{C}_{i_\mathbb{k}}}$ can be defined as the points on the contour of $\mathbb{C}_i$ between the points of intersection. We assume that the splitting points on a clump $\mathbb{C}_i$ commonly occur at $(\mathbb{B}_{\mathbb{C}_i} \cup \mathbb{F}_{\mathbb{C}_i})$ where $\mathbb{F}_{SA_{\mathbb{C}_i}} = \left\{\cup_{\mathbb{k}=1}^{\mathbb{K}} \mathbb{F}_{\mathbb{C}_{i_\mathbb{k}}}\right\}$ and $\mathbb{B}_{\mathbb{C}_i} = \left\{\cup_{\mathbb{k}=1}^{\mathbb{K}} \mathbb{B}_{\mathbb{C}_{i_\mathbb{k}}}\right\}$ is defined as the boundary of the $\mathbb{C}_i$ and $SA_{\mathbb{C}_i}$ (such as the red line in Fig. 5). In this work, the invalid splitting areas are ignored using the method proposed in [59].

The distance between the vertices of a splitting line should be small relative to the distance between the vertices along the contour of the shape, [60,61]. To determine the splitting point pairs, let $(\mathbf{A}, \mathbf{B}) \in \mathbb{S}$ where $\mathbb{S} = \left\{(\mathbf{A}, \mathbf{B}) | \mathbf{A} \in \mathbb{B}_{\mathbb{C}_{i_\mathbb{h}}}, \mathbf{B} \in \left(\mathbb{B}_{\mathbb{C}_{i_\mathbb{j}}} \cup \mathbb{F}_{\mathbb{C}_{i_\mathbb{h}}}\right) \text{for} \quad 1 \le \mathbb{h}, \mathbb{j} \le \mathbb{K} \quad \text{and} \quad \mathbb{h} \ne \mathbb{j}\right\}$, the cost function between points **A** and **B** can be defined as follows:

$$E_s(\mathbf{A}, \mathbf{B}) = \frac{\text{dist}(\mathbf{A}, \mathbf{B})}{\min \text{Length}(\mathbf{A}, \mathbf{B}), \text{Length}(\mathbf{B}, \mathbf{A})} \tag{26}$$

where dist(**A**,**B**) denotes the Euclidean distance between **A** and **B** and Length (**A**, **B**) represents the clockwise length from point **A** to **B** on the boundary of the segmented cell. The pair of splitting point positions can be obtained using the following minimization (see Fig. 6c):

$$(\mathbf{A}^*, \mathbf{B}^*) = \arg \min_{\mathbf{A},\mathbf{B}} E_s(\mathbf{A}, \mathbf{B}) \tag{27}$$

In order to acquire the appropriate splitting point-pair, at each iteration, a list of the ten splitting point-pairs are sorted in increasing order according to their value of the E_s. The splitting point-pair whose E_s is smaller than the others, is set as the first candidate. Then, the following conditions are utilized [61]. 1) The area ratio of the two parts resulting from the separation using the straight line should be among a certain range, and 2) compared with the length of the maximum local chord of the$\mathbb{C}_i$, the length of the separation line should be smaller. Once a splitting point-pair has been found to satisfy the conditions, it will be taken as the desired splitting point positions $(\mathbf{A}^*, \mathbf{B}^*)$.

2.3.3. Cut between selected points on local image patch manifold

Most of the existing methods have only used the binarized image which is a result of the segmentation procedure, and so have ignored the properties of the original image in splitting line formation. Basically this means taking a cut with the smallest Euclidean distance between $\mathbf{A}^*$and $\mathbf{B}^*$. Although the given clump might be separated into their correct number of constituent objects, it may not give the correct individual cell areas. Therefore, the properties of image pixels can be used to form the accurate splitting line [60]. These properties can be obtained from different

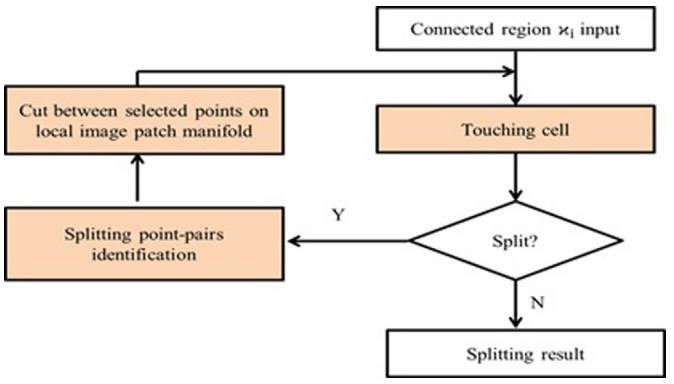

Fig. 4. Flowchart of the utilized three-step splitting method.

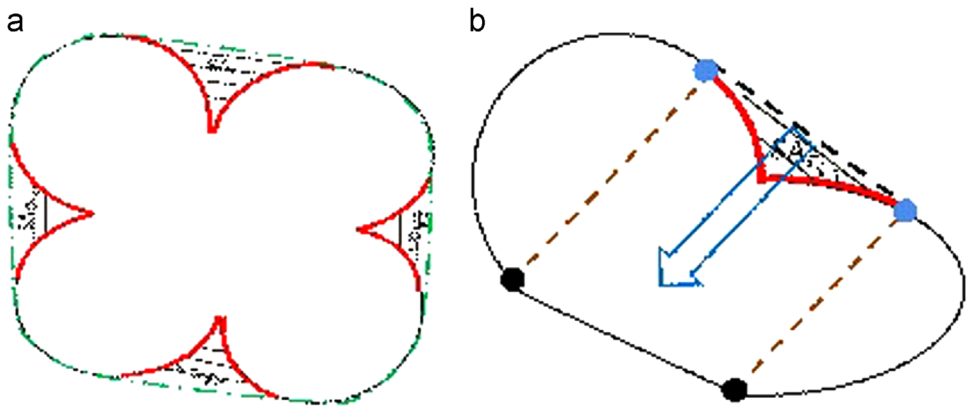

Fig. 5. (a) An overlapping clump with $\mathbb{k} > 1$ and the morphological properties that are used in our splitting algorithm. The dashed green line indicates the convex hull region, the white regions are the area of the cell, the hatched regions are splitting areas, the red line present the boundary of the $\mathbb{C}_i$ and $SA_{\mathbb{C}_i}$. (b) An overlapping clump with $\mathbb{k} = 1$. The dashed black line indicates the local chord, the blue arrow is the orientation of directional vector associated with the local chord, blue circles show points on the tails of the local chord, the dashed brown lines are the lines initiated from the tails of the local chord aligned in the same direction as the directional vector, and black circles indicate intersection points.

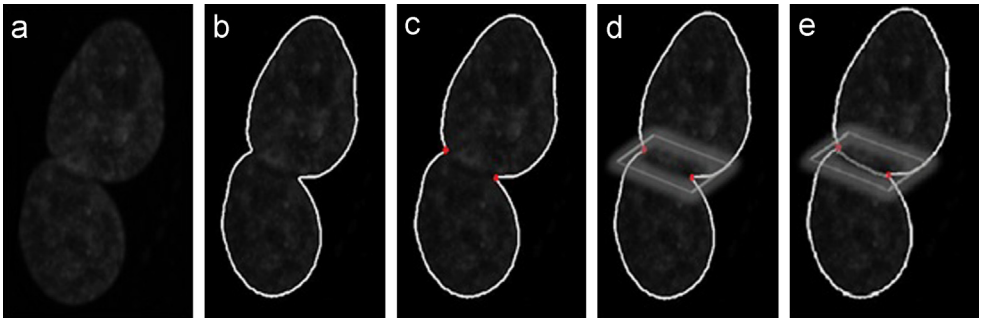

Fig. 6. Visual results for cell splitting. (a) original image, (b) segmented image, (c) splitting point-pair, (d) local image patch (the parallelogram area highlighted), (e) the splitting result.

information channels. For instance, while the intensity of a pixel could be directly acquired from the original image, the local spatial information and texture information are obtained from the processed image. For splitting line formation, let $\mathbb{I} \rightarrow \mathbb{R}^{\mathbb{v}}$ denotes a given image with the properties obtained from different information channels, where $\mathbb{v}$ is the dimension of the data point. To form the splitting line, image intensity as well as the filtered intensity of the pixels, which represents the local spatial information, are utilized. The filtered intensity of pixel is the mean filtered intensity using a 3×3 window. Using the local spatial information is helpful in obtaining a more accurate splitting line for the fluorescence microscopy images with intensity inhomogeneity. For given $\mathbf{A}^*$and $\mathbf{B}^*$ in the image domain Ω, the image patch around them (see Fig. 6d) can be denoted as follows:

$$\mathbb{P}_{\mathbf{A}^*\mathbf{B}^*} = (\mathbb{I}(\mathbf{y}), \mathbf{y} \in \mathbb{N}_{\mathbf{A}^*\mathbf{B}^*} \tag{28}$$

where $N_{\mathbf{A}^*\mathbf{B}^*}$ can be considered as a joint neighbourhood of points $\mathbf{A}^*$and $\mathbf{B}^*$ and the size of $\mathbb{N}_{\mathbf{A}^*\mathbf{B}^*}$ is proportional to the object size. The surface manifold of image patch $\mathbb{P}_{\mathbf{A}^*\mathbf{B}^*}$ can be defined as follows:

$$\mathbb{P}^{m}{}_{\mathbf{A}^*\mathbf{B}^*} = ((\mathbf{y}, \mathbb{I}(\mathbf{y})), \mathbf{y} \in \mathbb{N}_{\mathbf{A}^*\mathbf{B}^*}) \tag{29}$$

where the superscript m denotes the surface manifold of patch $\mathbb{P}$. The aim is to find the shortest path on the image patch surface manifold $\mathbb{P}^{m}{}_{\mathbf{A}^*\mathbf{B}^*}$ that connects the two splitting points in the local image patch $\mathbb{P}^{m}{}_{\mathbf{A}^*\mathbf{B}^*}$.

We use the geodesic distance as a distance metric $d_m(\mathbf{A}^*, \mathbf{B}^*)$ to measure the length of the shortest path on the manifold connecting the two splitting points $\mathbf{A}^*$and $\mathbf{B}^*$ on the image patch surface manifold $\mathbb{P}^{m}{}_{\mathbf{A}^*\mathbf{B}^*}$. Let the metric tensor G [62] be defined with the following elements:

$$g_{i,j} = \alpha_i \Delta_{i,j} + \sum_{k=1}^{\mathbb{v}} \beta_k^2 \frac{\partial \mathbb{I}_k}{\partial y_i} \frac{\partial \mathbb{I}_k}{\partial y_j} \tag{30}$$

where $i, j \in 1, 2$ and $\Delta_{i,j}$ denotes the Kronecker Delta. α_i and β_k are parameters that are used to tune the influence of Euclidean distances and image values, respectively, on the distance measure. In this study, we set $\alpha_i = \frac{1}{d_i}$ and $\beta_k = \frac{s}{r_k}$ in which d_i denotes the range of the image in the ith spatial dimension, r_k denotes the dynamic range of the kth image value, and s is a constant which is defaulted to $s = 1$. The role of s here is to balance the overall effect of the spatial distance and intensity value in the distance computation. Measuring the geodesic distance for infinitesimal changes in Y can be done by using the metric tensor G. The arc length for a curve $c(\tau)$ from $Y_1 = c(a)$ to $Y_2 = c(b)$ is measured by:

$$L = \int_a^b \sqrt{\sum_{i,j=1}^{2} \Delta_{i,j}(c(\tau)) \left(\frac{dY_i}{dt} c(\tau)\right) \left(\frac{dY_j}{dt} c(\tau)\right)} dt \tag{31}$$

(31) can be minimized using a geodesic curve.

Fig. 6 illustrates the process of finding the weighted shortest path between $\mathbf{A}^*$ and $\mathbf{B}^*$ on $\mathbb{P}^{m}{}_{\mathbf{A}^*\mathbf{B}^*}$. It can be solved iteratively using Dijkstra's algorithm in O(NlogN) time [15]. It is important to note that when the image information is not adequate, the cut between points $\mathbf{A}^*$ and $\mathbf{B}^*$ will degenerate to the shortest Euclidean distance between the splitting points, which is the same result as for most other existing approaches.

3. Experimental results

The proposed approach is applied to 2D fluorescence microscopy images of cell nuclei from four experiments which includes different cell types. Two data sets from [63] which have ground truth are used. The first data set consists of 48 images, each with a size of 1349×1030 pixels and has 1831 U20S Hoechst stained cell nuclei (see Fig. 7a). The second data set contains 49 images, each with a size of 1344×1024 pixels and has 2178 NIH3T3 Hoechst stained cell nuclei (see Fig. 7b). It is noted that since the images of the second data set suffer from intensity inhomogeneity, in comparison with the images in the first set, automatic analysis of the second set is more challenging. We also used images from BBBC005 [64]. The data set consists of 17 images, each with a size of 520 × 696 pixels and has approximately 159 cell nuclei (see Fig. 7c). Finally, the set of synthetic images of cell populations with realistic properties generated with the SIMCEP simulation tool [65] is also used. The SIMCEP simulation tool is available from http://www.cs.tut.fi/sgn/csb/simcep/. The generated set includes 20 simulated images of cell populations with ground truth, each with a size of 400×400 pixels and includes approximately 400 cell nuclei (see Fig. 7d).

The performance of the LLBWIP algorithm is evaluated using region-based and contour-based measures. For region-based measure, the Jaccard coefficient [66], which is widely used to measure spatial overlap, as well as Dice false positive (Dice FP) and Dice false negative (Dice FN) are used. The Dice FP is used to measure the over-segmentation and Dice FN gives a measure of under-segmentation. For contour-based measures, the Hausdorff distance and mean absolute contour distance (MAD) are used. The Jaccard coefficient can be calculated as:

$$\text{Jaccard}(R, S) = \frac{|R \cap S|}{|R \cup S| \times 100} \tag{32}$$

where R is the binary reference image and S is the binary segmented image. The Dice FP and Dice FN are obtained using the following equation:

$$\text{DiceFP}(R, S) = \frac{2|\overline{R} \cap S|}{|R| + |S| \times 100} \tag{33}$$

$$\text{DiceFN}(R, S) = \frac{2|R \cap \overline{S}|}{|R| + |S| \times 100} \tag{34}$$

where $\overline{R}$ and $\overline{S}$ are the complements of the R and S respectively.

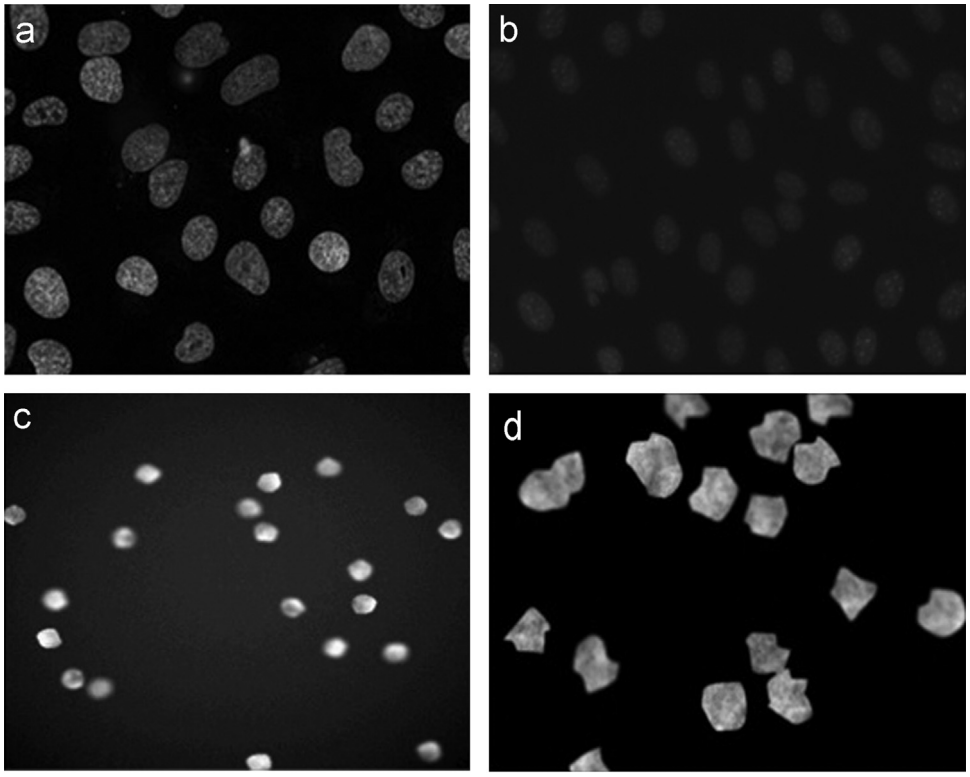

Fig. 7. Original images of the four different data sets. (a) U20S cells, (b) NIH3T3 cells, (c) BBBC005, (d) synthetic microscopy images from SIMCEP.

Table 1
Quantitative results for U20S data set for the different segmentation approaches.

Approach	U20S cells (48 images)				
	Jaccard	MAD	Hausdorff	Dice FP	Dice FN
MA[2]	83.8	4.6	13.6	8.3	9.7
WA [68]	52.4	11.2	34.1	30.5	31.5
OT [67]	76.1	11.7	33.9	12.7	13.3
BLS [23]	77.6	8.3	24.1	11.8	12.2
RSFE [25]	71.7	6.4	19.4	15.6	16.4
DRLSE [53]	72.9	7.8	21.3	15.3	14.7
Two-step [46]	88.7	4.2	12.8	5.4	7.1
Three-step [46]	88.4	4.7	13.4	5.3	5.2
LSBR [14]	83.2	5.8	19.8	11.8	9.1
LLBWIP	**91.6**	**3.5**	**12.7**	**4.7**	**3.9**

The best results are indicated by bold values.

The Hausdorff distance can be calculated as:

$$\text{Hausdorff}(R,S) = \max_{i \in S_c} D(i) \tag{35}$$

where $D(i)$ denotes the minimal Euclidean distance of pixel i to the contour of the reference object and S_c denotes the contour of the segmented object. For all n_{S_c} pixels on S_c, the MAD is defined as:

$$\text{MAD} = \frac{1}{n_{S_c}} \sum_{i \in S_c} |D(i)| \tag{36}$$

The performance of the splitting algorithm is evaluated using two detection measures, namely the number of false positives (FP) and the number of false negatives (FN). FP corresponds to spuriously segmented nuclei and FN corresponds to nuclei that have not been segmented.

Table 1 shows the quantitative results for the different performance measures which are averaged over all images in the U20S cells. The quantitative results for NIH3T3 cells are reported in Table 2 while the quantitative results for BBBC005 cells are reported in Table 3. Table 4 reports the quantitative results for synthetic cells. The splitting results are reported in Table 5. As a comparison, we also reported the results of the Merging algorithm (MA) [2], the Otsu thresholding (OT) [67], the Watershed algorithm (WA) [68], and level set-based methods, namely the Bayesian based level set approach (BLS) [23], the region-scalable fitting energy functional (RSFE) [25], the distance regularized level set method (DRLSE) [53], two step and three step approaches [46] and the level set method based on the Bayesian risk (LSBR) [14]. To evaluate the utilized three step splitting algorithm, its performance is compared with rule-based splitting method (RB) [59], improved clump splitting method (IM) [69], Watershed algorithm (WA), and two step and three step approaches [46]. It is noted that for RB and IM, the segmentation result of LLBWIP is utilized.

As can be seen from Tables 1 and 2, our approach obtains the best results for the Jaccard coefficient, Hausdorff distance, MAD, Dice FP, and Dice FN for the U20S data set. Furthermore, our approach yields better results than the level set based approaches. Note that for the Dice FP value and the Dice FN value, our approach yields significantly smaller values. LLBWIP also obtains the best results for the Jaccard coefficient, MAD, Dice FP, and Dice FN for the NIH3T3 data set. For the Hausdorff distance the best result is obtained by Two-step approach, although the result of the proposed approach is very close.

As can be seen from Tables 3 and 4, for the BBBC005 cells, LLBWIP yields significantly better results for the MAD, Hausdorff distance and Dice FN. In particular, for the BBBC005 images, we obtain a significantly smaller Dice FN value. For the Jaccard coefficient and Dice FP the best results are obtained by Two-step approach and MA, respectively, while the results of LLBWIP are very close behind. For the synthetic cell images, the best result for the Dice FN value is obtained by LSBR but our approach is only slightly poorer. However, the proposed approach has a significantly smaller Dice FP value. LLBWIP obtains significantly better results for the Jaccard coefficient, MAD, and Hausdorff distance.

Table 2
Quantitative results for NIH3T3 cells data set for the different segmentation approaches.

Approach	NIH3T3 cells (49 images)				
	Jaccard	MAD	Hausdorff	Dice FP	Dice FN
MA [2]	53.4	6.2	18.7	28.2	31.7
WA [68]	45.2	5.9	19.1	35.4	40.5
OT [67]	47.3	12.6	37.4	38.4	33.5
BLS [23]	61.2	7.5	22.2	26.1	22.9
RSFE [25]	62.8	6.8	21.5	20.4	23.5
DRLSE [53]	61.6	7.8	23.3	25.3	23.7
Two-step [46]	73.9	4.4	**14.2**	16.4	13.5
Three-step [46]	70.8	5.7	16.4	15.5	19.7
LSBR [14]	64.2	7.2	19.8	21.2	20.4
LLBWIP	**75.9**	**4.1**	14.3	**12.7**	**12.2**

The best results are indicated by bold values.

Table 3
Quantitative results for BBBC005 data set for the different segmentation approaches.

Approach	BBBC005 cells (17 images)				
	Jaccard	MAD	Hausdorff	Dice FP	Dice FN
MA [2]	80.4	1.3	5.8	**8.0**	12.9
WA [68]	75.3	**1.1**	5.0	13.1	17.8
OT [67]	76.0	2.3	5.4	14.1	13.9
BLS [23]	68.0	2.4	4.6	18.4	21.5
RSFE [25]	70.6	1.5	7.0	17.7	19.6
DRLSE [53]	70.4	2.7	4.9	18.9	16.7
Two-step [46]	**85.6**	**1.1**	3.6	**7.7**	8.4
Three-step [46]	83.2	1.5	3.9	10.7	9.1
LSBR [14]	75.2	1.9	4.7	14.2	15.9
LLBWIP	83.4	**1.1**	**3.5**	8.3	**7.2**

The best results are indicated by bold values.

Table 4
Quantitative results for synthetic data set for the different segmentation approaches.

Approach	Synthetic cells (20 images)				
	Jaccard	MAD	Hausdorff	Dice FP	Dice FN
MA [2]	65.2	1.6	5.1	18.6	24.5
WA [68]	64.5	1.2	5.6	22.3	21.8
OT [67]	63.2	1.7	7.4	22.7	24.2
BLS [23]	72.4	0.9	4.8	15.4	18.5
RSFE [25]	69.5	1.5	7.1	20.4	15.5
DRLSE [53]	62.0	1.3	6.7	22.9	23.0
Two-step [46]	76.7	1.2	4.8	12.7	13.4
Three-step [46]	73.1	1.4	5.3	13.2	16.7
LSBR [14]	74.6	1.4	4.1	18.1	**10.9**
LLBWIP	**83.3**	**0.8**	**3.7**	**10.1**	11.8

The best results are indicated by bold values.

As can be seen from Table 5, the proposed splitting approach yields the best results for the U20S cells and the NIH3T3 cells. The obtained results are better than the best results in the evaluation studies proposed in [46,63]. For the BBBC005 cells, the best value for the FP is obtained by RB, while we obtain intermediate result. In particular, for the BBBC005 cells, we obtained significantly smaller value for the FN value. For the synthetic cells, the proposed splitting approach, yields best results for the FN value. Regarding the FP value, the best result is obtained by the WA, while the obtained result by the proposed splitting approach is only slightly poorer.

For each data set, the ranking of the algorithms according to the values obtained by Jaccard, Hausdorff distance, and MAD, is depicted in Table 6. For each metric, the differences between the methods are only considered statistically significant if the 95% confidence intervals of the estimate of the true means do not overlap. To acquire the ranking for each data set 135 t-tests are performed (45 possible pairings of the methods for each of the 3 metrics). Bonferroni correction of the confidence intervals is used to adjust for multiple comparisons.

Table 5
Quantitative results for different data sets for the different splitting approaches.

Approach	U20S cells		NIH3T3 cells		BBBC005 cells		Synthetic cells	
	FP	FN	FP	FN	FP	FN	FP	FN
WA [68]	1.9	3.0	11.6	5.5	1.9	2.8	**3.4**	5.7
RB [59]	0.5	3.3	2.6	5.5	**1.1**	2.7	4.8	3.9
IM [69]	0.7	2.9	3.9	5.2	2.6	4.1	3.5	4.1
Two-step [46]	0.5	3.8	2.8	6.1	1.7	5.3	4.7	5
Three-step [46]	0.5	3.9	1.7	11.3	1.8	4.9	6.1	4.7
Proposed approach	**0.3**	**2.7**	**1.5**	**5**	1.7	**2.4**	3.5	**3.6**

The best results are indicated by bold values.

All experiments are performed using Matlab on a 64-bit Windows machine, which has a Intel core i7 CPU 2640 M, 2.8 GHz, with 8 GB RAM. Selection of the value of q is critical. The performance of our algorithm increases with the increase of the size of $q \times q$ neighbourhood. For larger value of q ($q=5$), our approach yields better results, while the time cost also increased significantly. Taking both the segmentation performance and the computation time into consideration, we suggest $3 \le q \le 4$. It is important to note that all the level set based approaches use the standard level set scheme with gradient descent optimization and the convergence criterion is defined as the MAD between the contours of segmented objects in two consecutive iterations. In this work, γ, y_1, y_2 are set to $255\times255\times10^{-3}$, 6, and 92×10^{-2}, respectively. For U20S date set, BBBC005 data set, and synthetic cells, we set $\varepsilon = 1$. For NIH3T3 data set, we set $\varepsilon = 1.5$. Based on the performed analysis in [70], for a given $n \times n$ image, the computational complexity of a level set model is $O(n^2)$ for each evolving level set. LLBWIP uses information of the image patches which would increase the computational cost. However, since $q \le n$ and q is fixed in LLBWIP, the computational complexity of LLBWIP can be approximated by $O(n^2)$. To facilitate reproducible research and to enable future comparison with other methods, we will make our code freely available for other researchers.

4. Conclusion

Accurate automated cell-nuclei segmentation in fluorescence microscopy images is important in high throughput cell study. A novel algorithm for cell-nuclei image segmentation has been introduced in this paper. For the level sets segmentation, we have developed LLBWIP as a novel local energy functional based on the Bayesian classification risk for an image patch. A weighting scheme is used to enable the pixels in each image patch to have anisotropic weights in the local energy functional. The final energy functional is then obtained by integrating the local energy over the entire image domain. For cells that are touching, a three-step touching-cell splitting algorithm has been proposed for cell splitting. Our cell splitting algorithm utilizes the image properties from different information channels to define the surface manifold of the image patch and form the optimum splitting line. The performance of the proposed algorithms has been validated extensively on four fluorescence microscopy image data sets containing

Table 6
Ranking of segmentation methods according to the Jaccard, Hausdorff distance and MAD metrics.

Data set	Metric	Ranking
U20S	Jaccard	LLBWIP > Two-step= Three-step > MA= LSBR > BLS = OT = DRLSE = RSFE > WA
	MAD	LLBWIP > Two-step > MA > Three-step > LSBR > RSFE > DRLSE = BLS > WA = OT
	Hausdorff	LLBWIP = Two-step > Three-step = MA > RSFE=LSBR = DRLSE > BLS > WA = OT
NIH3T3	Jaccard	LLBWIP > Two-step > Three-step > LSBR > RSFE = DRLSE = BLS > MA > WA = OT
	MAD	LLBWIP= Two-step > Three-step > WA = MA = RSFE > LSBR=BLS = DRLSE > OT
	Hausdorff	Two-step =LLBWIP > Three-step > MA = WA > LSBR > RSFE = BLS = DRLSE > OT
BBBC005	Jaccard	Two-step > LLBWIP= Three-step > MA > OT = WA= LSBR > RSFE = DRLSE = BLS
	MAD	LLBWIP = WA = Two-step = Three-step= MA > RSFE > LSBR > BLS > OT > DRLSE
	Hausdorff	LLBWIP= Two-step > Three-step > BLS = LSBR > DRLSE > WA = OT = MA > RSFE
Synthetic cells	Jaccard	LLBWIP > Two-step > Three-step = LSBR > BLS = RSFE > MA= WA = OT = DRLSE
	MAD	LLBWIP = BLS > Two-step = WA > LSBR= DRLSE = Three-step = RSFE > RSFE= OT
	Hausdorff	LLBWIP > LSBR > Two-step = BLS > MA= Three-step > WA > DRLSE = RSFE > OT

different cell types. Experiments demonstrated that the proposed approaches are robust and capable of producing significantly more accurate segmentation results than many state-of-the-art approaches we compared with. However, similar to most level sets approaches, the proposed segmentation algorithm has a non-convex energy functional. Therefore, it could suffer from local minima and poor initialization. Our future research effort will concentrate on overcoming these defficiencies.

Conflict of interest

None declared.

Acknowledgments

This work was supported by Australian Research Council (ARC) Discovery Grant DP1097059 and Griffith International Post-graduate Research Scholarship (GUIPRS).

References

[1] C. Wählby, J. Lindblad, M. Vondrus, E. Bengtsson, L. Björkesten, Algorithms for cytoplasm segmentation of fluorescence labelled cells, Anal. Cell. Pathol. 24 (2002) 101–111.
[2] G. Lin, U. Adiga, K. Olson, J.F. Guzowski, C.A. Barnes, B. Roysam, A hybrid 3D watershed algorithm incorporating gradient cues and object models for automatic segmentation of nuclei in confocal image stacks, Cytom. Part A 56 (2003) 23–36.
[3] J. Cheng, J.C. Rajapakse, Segmentation of clustered nuclei with shape markers and marking function, Biomed. Eng. IEEE Trans. 56 (2009) 741–748.
[4] B. Chen, Q. Zou, Y. Li, A new image segmentation model with local statistical characters based on variance minimization, Appl. Math. Model. 39 (2015) 3227–3235.
[5] L. Wang, Y. Chen, X. Pan, X. Hong, D. Xia, Level set segmentation of brain magnetic resonance images based on local Gaussian distribution fitting energy, J. Neurosci. Methods 188 (2010) 316–325.
[6] L. Wang, L. He, A. Mishra, C. Li, Active contours driven by local Gaussian distribution fitting energy, Signal Process. 89 (2009) 2435–2447.
[7] X.F. Wang, D.S. Huang, H. Xu, An efficient local Chan–Vese model for image segmentation, Pattern Recognit. 43 (2010) 603–618.
[8] Z. Ji, Y. Xia, Q. Chen, Q. Sun, D. Xia, D.D. Feng, Fuzzy c-means clustering with weighted image patch for image segmentation, Appl. Soft Comput. 12 (2012) 1659–1667.
[9] S.P. Awate, R.T. Whitaker, Unsupervised, information-theoretic, adaptive image filtering for image restoration, Pattern Anal. Mach. Intell. IEEE Trans. 28 (2006) 364–376.
[10] Y.L. Liu, J. Wang, X. Chen, Y.W. Guo, Q.-S. Peng, A robust and fast non-local means algorithm for image denoising, J. Comput. Sci. Technol. 23 (2008) 270–279.
[11] T. Weissman, E. Ordentlich, G. Seroussi, S. Verdú, M.J. Weinberger, Universal discrete denoising: Known channel, Inf. Theory IEEE Trans. 51 (2005) 5–28.
[12] G. Cassela, R. Berger, Statistical inference, 1990.
[13] R.N. Strickland, Image-processing techniques for tumor detection, CRC Press, United States, Florida, 2002.
[14] Y.T. Chen, A level set method based on the Bayesian risk for medical image segmentation, Pattern Recognit. 43 (2010) 3699–3711.
[15] E.W. Dijkstra, A note on two problems in connexion with graphs, Numer. Math. 1 (1959) 269–271.
[16] C. Jung, C. Kim, Segmenting clustered nuclei using H-minima transform-based marker extraction and contour parameterization, Biomed. Eng. IEEE Trans. 57 (2010) 2600–2604.
[17] M. Kass, A. Witkin, D. Terzopoulos, Snakes: active contour models, Int. J. Comput. Vis. 1 (1988) 321–331.
[18] C. Zimmer, J.-C. Olivo-Marin, Coupled parametric active contours, Pattern Anal. Mach. Intell. IEEE Trans. 27 (2005) 1838–1842.
[19] X. Wang, W. He, D. Metaxas, R. Mathew, E. White, Cell segmentation and tracking using texture-adaptive snakes, in: Biomed. Imaging From Nano to Macro, ISBI, 4th IEEE Int. Symp., IEEE, 2007, pp. 101–104.
[20] M. Butenuth, C. Heipke, Network snakes: graph-based object delineation with active contour models, Mach. Vis. Appl. 23 (2012) 91–109.
[21] S. Osher, J.A. Sethian, Fronts propagating with curvature-dependent speed: algorithms based on Hamilton-Jacobi formulations, J. Comput. Phys. 79 (1988) 12–49.
[22] T.F. Chan, L. Vese, Active contours without edges, Image Process. IEEE Trans. 10 (2001) 266–277.
[23] M. Rousson, R. Deriche, A variational framework for active and adaptative segmentation of vector valued images, in: Proceedings of the Motion Video Comput. Work., IEEE, 2002, pp. 56–61.
[24] C. Li, C.Y. Kao, J.C. Gore, Z. Ding, Implicit active contours driven by local binary fitting energy, in: Comput. Vis. Pattern Recognition, CVPR'07. IEEE Conf., IEEE, 2007, pp. 1–7.
[25] C. Li, C.Y. Kao, J.C. Gore, Z. Ding, Minimization of region-scalable fitting energy for image segmentation, Image Process. IEEE Trans. 17 (2008) 1940–1949.
[26] X. Bresson, S. Esedoğlu, P. Vandergheynst, J.-P. Thiran, S. Osher, Fast global minimization of the active contour/snake model, J. Math. Imaging Vis. 28 (2007) 151–167.
[27] T.F. Chan, L.A. Vese, Active contour and segmentation models using geometric PDE's for medical imaging Geometric Methods Bio-Medical Image Process, Springer, 2002, pp. 63–75.
[28] A. Tsai, A. Yezzi Jr, A.S. Willsky, Curve evolution implementation of the Mumford–Shah functional for image segmentation, denoising, interpolation, and magnification, Image Process. IEEE Trans. 10 (2001) 1169–1186.
[29] C. Ortiz de Solorzano, R. Malladi, S.A. Lelievre, S.J. Lockett, Segmentation of nuclei and cells using membrane related protein markers, J. Microsc. 201 (2001) 404–415.
[30] A. Dufour, V. Shinin, S. Tajbakhsh, N. Guillén-Aghion, J.-C. Olivo-Marin, C. Zimmer, Segmenting and tracking fluorescent cells in dynamic 3-D microscopy with coupled active surfaces, Image Process. IEEE Trans. 14 (2005) 1396–1410.
[31] S.K. Nath, K. Palaniappan, F. Bunyak, Cell segmentation using coupled level sets and graph-vertex coloring, in: Proceedings of the Medical Image Computing Computer-assisted Intervention, Springer, 2006, pp. 101–108.
[32] H. Chang, Q. Yang, B. Parvin, Segmentation of heterogeneous blob objects through voting and level set formulation, Pattern Recognit. Lett. 28 (2007) 1781–1787.
[33] K. Palaniappan, I. Ersoy, S.K. Nath, Moving object segmentation using the flux tensor for biological video microscopy, in: Proceedings of the Advances in Multimedia Information Processing, Springer, 2007, pp. 483–493.
[34] P. Yan, X. Zhou, M. Shah, S.T.C. Wong, Automatic segmentation of high-throughput RNAi fluorescent cellular images, Inf. Technol. Biomed. IEEE Trans. 12 (2008) 109–117.
[35] M. Maška, O. Daněk, C. Ortiz-de-Solórzano, A. Muñoz-Barrutia, M. Kozubek, I. F. García, A two-phase segmentation of cell nuclei using fast level set-like algorithms, in: Image Anal, Springer-Verlag, Berlin, Heidelberg, 2009, pp. 390–399.
[36] K. Mosaliganti, A. Gelas, A. Gouaillard, R. Noche, N. Obholzer, S. Megason, Detection of spatially correlated objects in 3d images using appearance models and coupled active contours, in: Proceedings of the Medical Image Computing Computer-assisted Intervention Springer, 2009, pp. 641–648.

[37] D. Padfield, J. Rittscher, N. Thomas, B. Roysam, Spatio-temporal cell cycle phase analysis using level sets and fast marching methods, Med. Image Anal. 13 (2009) 143–155.
[38] I. Ersoy, F. Bunyak, V. Chagin, M.C. Cardoso, K. Palaniappan, Segmentation and classification of cell cycle phases in fluorescence imaging, in: Proceedings of the Medical Image Computing Computer-assisted Intervention, Springer, 2009, pp. 617–624.
[39] O. Dzyubachyk, W. Van Cappellen, J. Essers, W.J. Niessen, E. Meijering, Advanced level-set-based cell tracking in time-lapse fluorescence microscopy, Med. Imaging, IEEE Trans. 29 (2010) 852–867.
[40] J. Xu, A. Janowczyk, S. Chandran, A. Madabhushi, A high-throughput active contour scheme for segmentation of histopathological imagery, Med. Image Anal. 15 (2011) 851–862.
[41] Z. Ma, R.M.N. Jorge, T. Mascarenhas, J.M.R.S. Tavares, Segmentation of female pelvic organs in axial magnetic resonance images using coupled geometric deformable models, Comput. Biol. Med. 43 (2013) 248–258.
[42] Z. Ma, R.N.M. Jorge, J.M.R.S. Tavares, A shape guided C–V model to segment the levator ani muscle in axial magnetic resonance images, Med. Eng. Phys. 32 (2010) 766–774.
[43] A. Gharipour, A.W.C. Liew, Colon cell image segmentation based on level set and kernel-based fuzzy clustering, in: Proceedings of the Intelligent Computing Theories and Technology, Springer, 2013, pp. 120–129.
[44] A. Gharipour, A.W.C. Liew, An integration strategy based on fuzzy clustering and level set method for cell image segmentation, in: Signal Processing Communication and Computing (ICSPCC), IEEE Int. Conf., IEEE, 2013, pp. 1–5.
[45] A. Gharipour, A.W.C. Liew, Fuzzy clustering using local and global region information for cell image segmentation, in: Fuzzy Syst. (FUZZ-IEEE), IEEE Int. Conf., IEEE, 2014, pp. 216–222.
[46] J.P. Bergeest, K. Rohr, Efficient globally optimal segmentation of cells in fluorescence microscopy images using level sets and convex energy functionals, Med. Image Anal. 16 (2012) 1436–1444.
[47] A.W.C. Liew, S.H. Leung, W.H. Lau, Fuzzy image clustering incorporating spatial continuity, IEE Proc.-Vision., Image Signal Process. 147 (2000) 185–192.
[48] A.W.C. Liew, H. Yan, An adaptive spatial fuzzy clustering algorithm for 3-D MR image segmentation, Med. Imaging, IEEE Trans. 22 (2003) 1063–1075.
[49] A.W.C. Liew, H. Yan, N.-F. Law, Image segmentation based on adaptive cluster prototype estimation, Fuzzy Syst. IEEE Trans. 13 (2005) 444–453.
[50] A.W.C. Liew, S.H. Leung, W.H. Lau, Segmentation of color lip images by spatial fuzzy clustering, Fuzzy Syst. IEEE Trans. 11 (2003) 542–549.
[51] N. Paragios, R. Deriche, Geodesic active regions and level set methods for supervised texture segmentation, Int. J. Comput. Vis. 46 (2002) 223–247.
[52] T.F. Li, An efficient algorithm to find the MLE of prior probabilities of a mixture in pattern recognition, Pattern Recognit. 29 (1996) 337–339.
[53] C. Li, C. Xu, C. Gui, M.D. Fox, Distance regularized level set evolution and its application to image segmentation, Image Process. IEEE Trans. 19 (2010) 3243–3254.
[54] H. Kong, M. Gurcan, K. Belkacem-Boussaid, Partitioning histopathological images: an integrated framework for supervised color-texture segmentation and cell splitting, Med. Imaging IEEE Trans. 30 (2011) 1661–1677.
[55] G. Loy, A. Zelinsky, Fast radial symmetry for detecting points of interest, Pattern Anal. Mach. Intell. IEEE Trans. 25 (2003) 959–973.
[56] W.X. Wang, Binary image segmentation of aggregates based on polygonal approximation and classification of concavities, Pattern Recognit. 31 (1998) 1503–1524.
[57] Q. Wen, H. Chang, B. Parvin, A Delaunay triangulation approach for segmenting clumps of nuclei, in: Biomedical Imaging From Nano to Macro, ISBI'09. IEEE Int. Symp., IEEE, 2009, pp. 9–12.
[58] M. Farhan, O. Yli-Harja, A. Niemistö, A novel method for splitting clumps of convex objects incorporating image intensity and using rectangular window-based concavity point-pair search, Pattern Recognit. 46 (2013) 741–751.
[59] S. Kumar, S.H. Ong, S. Ranganath, T.C. Ong, F.T. Chew, A rule-based approach for robust clump splitting, Pattern Recognit. 39 (2006) 1088–1098.
[60] H. Wang, H. Zhang, N. Ray, Clump splitting via bottleneck detection and shape classification, Pattern Recognit. 45 (2012) 2780–2787.
[61] W. Wang, Study on cell cluster splitting, in: Image and Graphics, ICIG, 4th Int. Conf., IEEE, 2007, pp. 427–431.
[62] S. Gallot, D. Hulin, J. Lafontaine, Riemannian geometry, Springer, 1990.
[63] L.P. Coelho, A. Shariff, R.F. Murphy, Nuclear segmentation in microscope cell images: a hand-segmented dataset and comparison of algorithms, in: Biomedical Imaging From Nano to Macro, ISBI'09. IEEE Int. Symp., IEEE, 2009, pp. 518–521.
[64] M.A. Bray, A.N. Fraser, T.P. Hasaka, A.E. Carpenter, Workflow and metrics for image quality control in large-scale high-content screens, J. Biomol. Screen. 17 (2012) 266–274.
[65] A. Lehmussola, P. Ruusuvuori, J. Selinummi, H. Huttunen, O. Yli-Harja, Computational framework for simulating fluorescence microscope images with cell populations, Med. Imaging, IEEE Trans. 26 (2007) 1010–1016.
[66] P. Jaccard, The distribution of the flora in the alpine zone, New Phytol. 11 (1912) 37–50.
[67] N. Otsu, A threshold selection method from gray-level histograms, Automatica 11 (1975) 23–27.
[68] L. Vincent, P. Soille, Watersheds in digital spaces: an efficient algorithm based on immersion simulations, IEEE Trans. Pattern Anal. Mach. Intell. (1991) 583–598.
[69] M. Farhan, O. Yli-Harja, A. Niemistö, An improved clump splitting method for convex objects, in: Proc. 7th Int. Work. Comput. Syst. Biol., 2010: pp. 35–38.
[70] D. Adalsteinsson, J.A. Sethian, A fast level set method for propagating interfaces, J. Comput. Phys. 118 (1995) 269–277.

Amin Gharipour received the Ph.D. degree from Griffith University, Australia. He is currently a Visiting Research Fellow in the School of Information & Communication Technology, Griffith University, Australia. His research interests include image processing, pattern recognition, and machine learning.

Alan Wee-Chung Liew is currently an Associate Professor with the School of Information & Communication Technology, Griffith University, Australia. His research interest is in the field of medical imaging, bioinformatics, computer vision, pattern recognition, and machine learning. He serves on the technical program committee of many international conferences and is on the editorial board of several journals, including the IEEE Transactions on Fuzzy Systems. He is a senior member of the IEEE since 2005.